Contact force calculation and evolution analysis of granular systems based on micro-CT experiment*

WANG Xiao, SONG Shiqi, PING Zijian, SHENG Siyuan, SHANG Xianyi, CHEN Fanxiu[1]

School of Science, Qingdao Technological University, Qingdao 266520, China

Abstract: The calculation of inter-granule contact force in three-dimensional (3D) granular systems is a key and challenging aspect of granular mechanics research. Two elastic rubber balls are used as research objects for in-situ flat pressing micro-CT experiments. Based on the Hertzian contact theory and Tatara large deformation contact theory, the contact model of elastic balls is verified, and the theoretical formula of the contact force of elastic balls based on the experiment is obtained. Taking the 3D granular systems as research object, *in-situ* probe loading experiment of micro-CT is carried out to obtain the 2D image sequence of the granules, after a series of digital transformations, the digital body images emerge, the contact force networks of the 3D granular systems under different loading conditions are obtained by constructing pore network models. The contact force distribution and evolution law of the granular systems are analyzed. The relation among the number of strong contacts, the distribution evolution, and the stability of the granular system is explored. The results show that the two elastic ball contact model conforms to the Hertzian contact theory and Tatara large deformation contact theory, and the contact force fitting formula based on experiment can characterize the contact force between two granules reasonably and effectively. The contact force of granules under probe loading is distributed in a net-like pattern starting from the contact point of the indenter and gradually transmitted to the lower and the surrounding area. The trend of average contact force is consistent with the trend of the contact times, showing a significant phase transition. With the increase of contact times, the frequency of particle compression increases, resulting in a greater contact force between granules, ultimately stabilizing at about 10.5 N. The number of strong contacts accounts for 45% to 50% of the total number of contacts, distributed throughout the whole granular system and supporting the network structure of the granular system. The larger values are concentrated below the indenter and exhibit a branching distribution. In the loading process, an equilibrium point is established at z = 14 mm, where the number of strong contacts reaches the peak. The network structure of strong contact force is spread throughout the entire 3D granular system, establishing the main skeleton that can withstand external loads. As the loading continues, the total value of strong contact forces increases, and their distribution

* The paper is an English translated version of the original Chinese paper published in *Acta Physica Sinica*. Please cite the paper as: WANG Xiao, SONG Shiqi, PING Zijian, SHENG Siyuan, SHANG Xianyi, CHEN Fanxiu. Contact force calculation and evolution analysis of granular systems based on micro-CT experiment, *Acta Physica Sinica* 2025, 74(1): 014501. doi: 10.7498/aps.74.20241206

1 Corresponding author: mecfx@163.com

within the granular system becomes more uniform.

Keywords: micro-CT，*in-situ* loading，contact model of granules，contact force

PACS: 45.70.–n, 62.20.–x, 41.50.+h, 06.30.Bp

doi: 10.7498/aps.74.20241206

cstr: 32037.14.aps.74.20241206

1. Introduction

Granular system[1–3] is a granular system composed of a large number of discrete particles. Particles form a complex contact network through discontinuous and non-uniform arrangement, which has complex characteristics between continuous and discontinuous media. When subjected to external forces, the contact forces between particles are transmitted step by step with the contact point as the carrier, and influence each other, which has the effect of pulling the trigger and moving the whole body. The macroscopic mechanical properties of three-dimensional granular systems are determined by the microscopic mechanical behavior of particles. Therefore, it is of great significance to calculate and study the contact force between particles as the basis for exploring the mechanical response of granular systems.

The experimental study of contact force in granular system is mainly divided into contact detection method and non-contact detection method. Contact detection methods, such as high-precision electronic balance weighing method [4], color sensitive carbon paper indentation method [5], etc., use tools to intervene in the internal detection of the contact force distribution at a certain position in the particle system, which causes certain interference to the particle system and affects the detection results. With the rapid development of data acquisition technology, laser technology and image processing technology, non-contact detection methods have emerged, such as photoelastic method [6], fluorescence confocal microscopy method [7] and magnetic resonance elastography method [8]. By determining the geometric position of particles, the structural characteristics of the system can be analyzed, and the three-dimensional contact force distribution information in the particle system can be obtained. In 2005, Majmudar and Behringer[9] carried out a series of two-dimensional particle loading experiments using photoelastic method; in 2009, Sanfratello *et al*[10] applied magnetic resonance elastography to the study of particle system and realized the visualization of particle structure in three-dimensional space; in 2016, Chen Fanxiu *et al*.[11] explored the dynamic law of particle system under concentrated force based on 2D-DIC; In 2022, Kondo et al.[12] conducted a pile model penetration test on the granular system based on digital image processing, and analyzed the load transfer and displacement changes of the particles during the test; In 2023, Wang Xiao et al.[13] used micro-CT to carry out in-situ loading experiments

on three-dimensional granular systems, and described the micro-mechanical behavior between particles in three-dimensional granular systems. The above research has carried out statistics and analysis on the mechanical law of granular system, the distribution and evolution of contact force, but has not obtained the specific contact force value. The calculation and research of contact force between particles is still the focus and difficulty in the field of granular matter mechanics.

Particle contact model is the theoretical basis for calculating the contact force between particles, and the related research and development are of leading significance to the study of the mechanical behavior of particle systems from the microscopic point of view. The research and development of particle contact model has a history of more than a hundred years, and has gradually formed a contact theory model suitable for different contact conditions and occasions. In 1881, Hertz[14] studied the small deformation spherical contact without adhesion, and solved the calculation model of small deformation spherical contact; in 1971, Johnson et al.[15] studied the small deformation ball contact adhesion problem based on Hertz model, that is, JKR adhesion model; in 1975, Derjaguin et al.[16] proposed that the equivalent normal load is the sum of normal load and adhesion, that is, DMT adhesion model; in 1991, Tatara et al.[17,18] proposed a theoretical model of rubber elastic spherical contact with nonlinear Young's coefficient and radial expansion of the contact surface; In 2008, He Siming et al.[19] proposed a new elastic-plastic contact theory of particles based on Hertz theory; In 2019, Yunruide and Dingbei[20] proposed a new contact model considering multi-scale contact state based on the classical Hertz contact mechanics theory and the existing fractal contact model; In 2023, Wu et al.[21] proposed a modified particle contact model for matching the ratio of uniaxial compressive strength to tensile strength of brittle rocks. At present, most of the existing particle contact models are based on idealized assumptions, which may be inconsistent with the actual situation in application. Therefore, it is necessary to combine experimental verification in the specific application of theoretical model calculation.

Micro-CT (micro-CT)[22–25] is a technology that uses X-ray beam to penetrate the measured object and forms a series of digital image sequences through the change of photoelectric signals. This technique is mostly used for nondestructive testing of the internal structure of objects, and in recent years it has been gradually applied to the[26,27] of the geometric characteristics and stress research of three-dimensional particle systems. Micro-CT provides a three-dimensional visualization model for the study of the mechanical properties of particle systems, which makes it possible to extract the contact information that is difficult to observe and quantify in three-dimensional particle systems, and provides a feasible experimental means for exploring the mechanical behavior of particles at the micro and mesoscopic levels.

In this paper, based on the micro-CT experiment, the contact model of double elastic particles is verified and the theoretical formula of contact force is obtained. The in-situ probe loading

experiment of three-dimensional elastic spherical particles is carried out. The three-dimensional digital model of the particle system is obtained through a series of digital changes, and the contact network model of the particles is constructed. The contact force between particles in the loading process is calculated based on the formula. This study will point out and describe the distribution and evolution of the contact force network in the three-dimensional granular system, and provide support for the identification and evolution analysis of the force chain[28] in the three-dimensional granular system.

2. Particle contact force model

2.1 Hertz contact theory

Hertz contact theory is a normal pressure contact theory of an isotropic elastic sphere under small deformation in the case of non-adhesion and frictionless, which was proposed by Hertz[14] in 1881. This theory explains the relationship between load, normal contact force and geometric deformation. It is assumed that there is a small circular contact region between two spherical particles, which is very small compared with the surface of the particles, and only elastic deformation occurs on the contact surface, and the contact force is perpendicular to the contact surface. As shown in Fig. 1, two spherical particles with radii of R are in elastic contact, and the normal contact force and contact area are calculated in equations (1) and (2).

$$F = \frac{4}{3}\frac{E}{1-v^2}\sqrt{R}\delta^{3/2}, \tag{1}$$

$$A = \pi a^2 = \pi R\delta, \tag{2}$$

Where F is the normal contact force between particles; δ is the amount of overlap between particles; A is the contact area between particles, a is the contact radius; R is the particle radius; E and v are the elastic modulus and Poisson's ratio of particles, respectively.

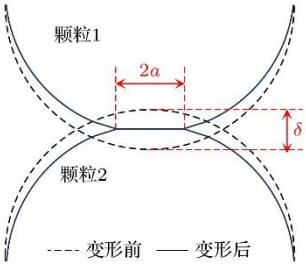

Figure 1. Hertz contact model.

(1) and (2) can be rewritten as (3) and (4):

$$F = \frac{4}{3}\frac{E}{(1-\upsilon^2)R}\left(\frac{A}{\pi}\right)^{3/2} = KA^{3/2}, \tag{3}$$

$$K = \frac{4}{3}\frac{E\pi^{-3/2}}{(1-\upsilon^2)R}, \tag{4}$$

Where K is the proportional coefficient of contact area to normal contact force, which is related to the elastic modulus, Poisson's ratio and diameter of the particle.

2.2 Tatara large deformation contact theory

Tatara's large deformation contact theory is a general theory of compression deformation of homogeneous non-viscous elastic spheres under large deformation[17]. This theory breaks through the two limitations of Hertz's contact theory, that is, the contact solid is only small deformation and linear elastic solid, and considers the behavior of nonlinear elastic materials based on Mooney's law of rubber deformation under large deformation.

In 1991, Tatara et al.[18] carried out uniaxial compression experiments on a 1 cm rubber elastic ball in a large deformation range, and measured the elastic displacement and contact radius of the rubber ball under an applied load of 10-5000 N. According to the experimental data of Tatara et al.[18], the relationship between the normal overlap δ of a single spherical particle and the contact force F is obtained, see Fig. 2.

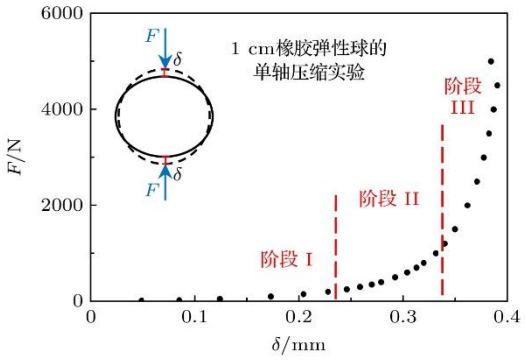

Figure 2. Relationship between normal overlap δ and contact force F for single granule.

It can be seen from Fig. 2 that the axial compression deformation of a single ball can be divided into three stages. Stage I is small deformation contact, and the calculation results are consistent with Hertz contact theory, that is, the contact force F is proportional to the 3/2 power of the normal overlap δ; Stage II is large deformation contact, and the power relationship between the contact force F and the normal overlap δ is raised to the third power; Stage II is super large deformation contact, while the power relationship between the contact force and the normal overlap is raised to the fifth power. The particle experiment of Tatara et al.[18] is based on the contact between a particle and a plane, which is only applicable to a

single spherical particle, and the normal overlap is calculated by the axial deformation of a single sphere. The actual particle system is the contact between two spherical surfaces, which is different from the particle experiment of Tatara et al.[18].

3. Micro-CT experiment

3.1 CT in situ loading experiment

The experimental equipment is a high-resolution integrated scanning and analysis system nanoVoxel-2792 produced by Tianjin Sanying Precision Co., Ltd. The CT system is shown in Fig. 3, which is mainly composed of a radiation source, a turntable and a detector. The loading device is an in-situ loading test system CT-020 based on the micro-CT design. The relative positions of the three are controlled by a screw rod and a stepping motor to adjust the imaging magnification. In the process of image acquisition, the X-ray emitted by the X-ray source passes through the loading device and the internal sample, and the detector receives the X-ray. The X-ray projection image obtained by one exposure is called two-dimensional digital radiography (DR) image, and the computed tomography (CT) imaging is called continuous shooting of multiple DR images during the rotation of the sample table and reconstruction of the three-dimensional spatial structure of the measured object. In the experiment, the micro-CT system uses the maximum tube voltage of 130 kV and the maximum current of 100 μA. The detector array is 1536 pixel × 1536 pixel, the effective imaging field of view is 130 mm × 130 mm, the exposure time is 0. 5 s, and the acquisition frame rate is 720 frame/s.

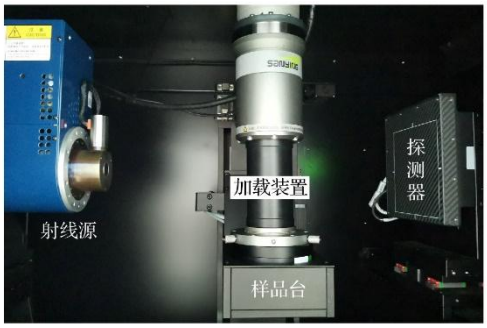

Figure 3. Micro-CT system.

In order to obtain the transmission of contact force in the particle system and ensure that the particles can move freely without being compacted, a cylindrical probe with a diameter of 1 cm and a height of 4 cm was used to load the experimental model, and 90 rubber elastic spheres with a diameter of 1 cm were used as the experimental objects. The experimental model is shown in Fig. 4, and the indenter and specimen of the in-situ loading test system are shown in Fig. 5. The experimental loading rate is 0.5 mm/min, and the image acquisition is carried out every 2 mm of the indenter.

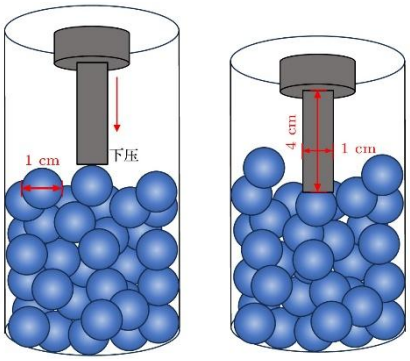

Figure 4. Test model.

Figure 5. Indenter and specimen.

3.2 Digital image processing

Digital image processing is a method and technology to reduce noise, enhance, restore, segment and extract information from the original image by computer[29–31]. The digital image processing involved in this experiment is mainly divided into four steps: image input, image preprocessing, image segmentation and information calculation and extraction. The specific process is shown in Fig. 6. 1) Image input: convert the photoelectric signal and digitize the image to obtain a series of DR two-dimensional images. 2) Image preprocessing: The image quality was improved by image enhancement and correction, and a series of DR images were combined and corrected by 3D reconstruction, and the reconstructed 3D digital image was obtained by mathematical operation. The number of voxels was 1500 × 1500 × 1500, and the voxel size VoxelDis was 0.0374 mm. 3) image segmentation: The gray data is extracted by threshold segmentation, and all the pixels in the gradient image are classified according to the gray value based on the watershed algorithm to complete the segmentation of the particle data. 4) Construct pore network model (PNM)[32,33] to calculate and extract information: calculate particle information and contact area based on PNM, and use the model to represent the particle contact network model, "pore" represents "particle", and "pore throat" represents "contact". Voxel coordinates and gray values are combined to extract particle information such as particle center of gravity coordinates, equivalent diameter, coordination number, etc. After the watershed algorithm is used to segment particle units, the particle contact area is

calculated based on the overlap of voxels at the contact position of two particle units.

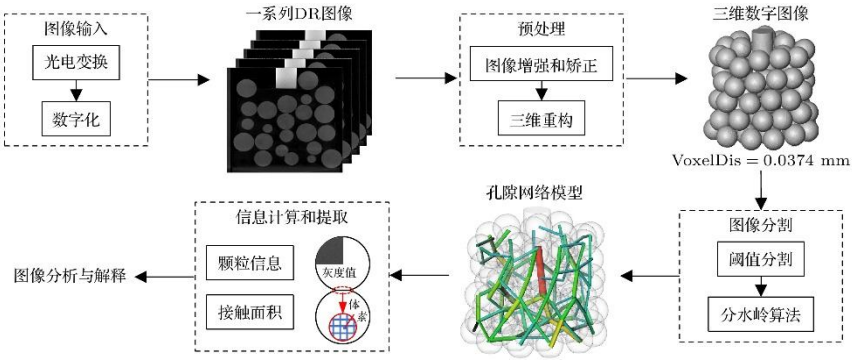

Figure 6. Image processing flow.

4. Validation of the contact model for bi-elastic particles.

The contact force and contact area between two rubber particles were obtained by micro-CT experiment of axial compression and scanning. Based on Hertz small deformation contact theory and Tatara large deformation contact theory, the elastic ball contact force formula of contact area and contact force was obtained by formula fitting.

4.1 Experimental model of double elastic particles

Based on Tatara's single sphere axial compression experiment, the experimental model was improved, and the two-sphere axial compression experiment was carried out to obtain the particle contact information with the help of micro-CT. The load P was applied to two rubber spheres with a diameter of 10 mm, and the angle between the center of the two spheres and the normal direction was θ. In order to ensure that the two particles basically maintain the axial direction and do not slide laterally with large displacement during uniaxial loading, the main force between the two particles is the normal contact force, and the particles are wrapped with sponge to limit the lateral displacement of the particles. In order to facilitate the subsequent image segmentation of the particle and the upper and lower indenters, the indenter and the particle are separated by a transparent acrylic sheet. The experimental model of the double elastic particle is shown in Fig. 7, and the indenter and sample of the in-situ loading test system are shown in Fig. 8.

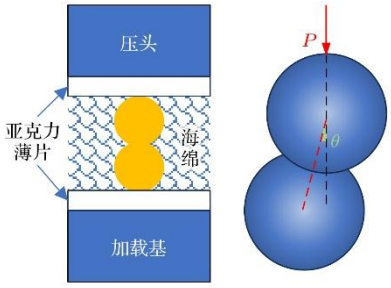

Figure 7. Experimental model of two granules.

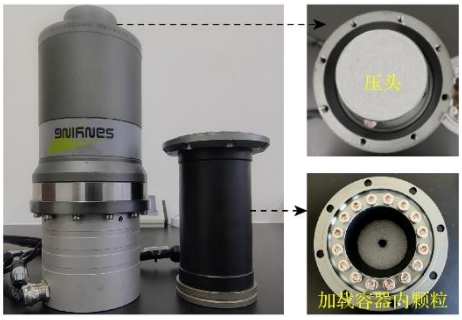

Figure 8. Indenter and specimen.

4.2 Loading Speed and Scanning Point Selection

Before the verification experiment, it is necessary to determine the appropriate loading speed and select the scanning points in advance to ensure that the scanning data can stably and effectively reflect the changes of the two-particle model during the loading process. The granular system was loaded continuously at four speeds of 0. 5, 1. 0, 1. 5 and 2. 0 mm/min, respectively, and the loading results showed that the change of speed had little effect on the *P*. In order to ensure that the change of particle state is more uniform and stable during the scanning process, the scanning loading speed is 0. 5 mm/min. According to the variation curve of *P*, 12 appropriate scanning points are selected at equal force intervals. See Fig. 9 for the variation of loading displacement *z* and applied load *P* at different speeds and the selection of scanning points. 12 groups of scanning points are selected.

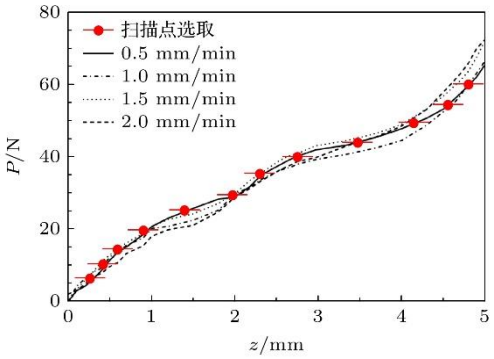

Figure 9. The *z*-*P* curves for two granules with different velocities.

4.3 Strain-contact force relation

During the loading process, the loading is suspended when the force value is loaded to the preset scanning point, and the scanning is started. After the scanning is finished, the loading is continued and the process is repeated. During the scanning process, due to the creep effect of the particles, the particles are unloaded, and the two particles may have an angle offset θ during the loading process, so there is a certain offset in the contact force before and after the scanning. See Fig. 10 for the relationship between the normal contact force *F* and the

strain ε before and after the scanning. It can be seen from Fig. 10 that the angle offset θ increases with the increase of strain ε, and the angle offset θ in this experiment is not more than 1.8 °, and the modified particle normal contact force is basically unchanged. The difference of particle contact force before and after scanning is about 5 N, and the difference does not change significantly with continuous loading scanning. The strain ε of the particle system is positively correlated with the contact force F, and with the increase of strain ε, the contact force F increases.

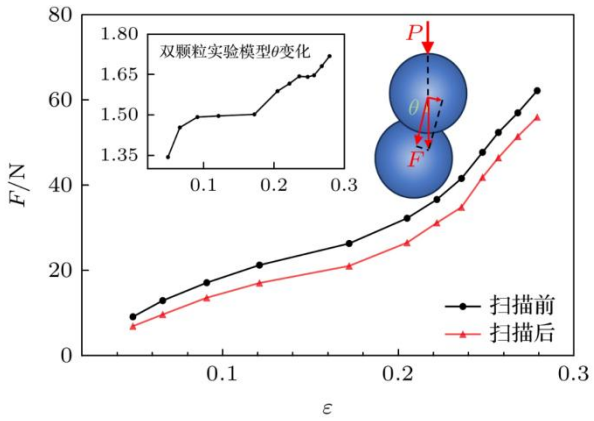

Figure 10. Relationship of strain ε and contact force *F*.

4.4 Strain-contact area relationship

Three-dimensional particle images were obtained by image processing, and a pore network model was established to calculate the contact area between two particles. Fig. 11 shows the relationship between strain ε and contact area A of the particle system at 12 scanning points. With the increase of strain ε, the contact area A increases linearly.

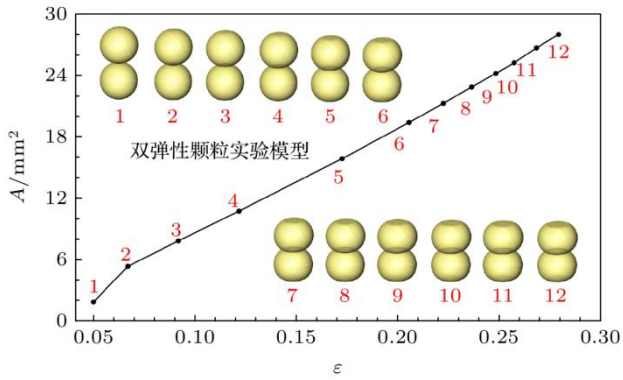

Figure 11. Relationship of strain ε and contact area A.

4.5 Contact Force Formula Fitting

During the probe loading state of the particle system, the strain and contact area of the two internal particles are in a small range, which are not more than the maximum strain and

contact area of the two-sphere axial compression experiment. Therefore, when the relationship between contact area A and contact force F is experimentally explored, the maximum strain ε = 28% and the maximum contact area A = 27.98 mm^2. The contact force before and after scanning was fitted by formula, and the fitting results and R^2 values were shown in Fig. 12. In order to ensure the uniqueness of the correspondence between the contact area and the contact force, the breakpoint of the piecewise fitting time (ε = 12.1%, A = 10.75) belongs to phase I only.

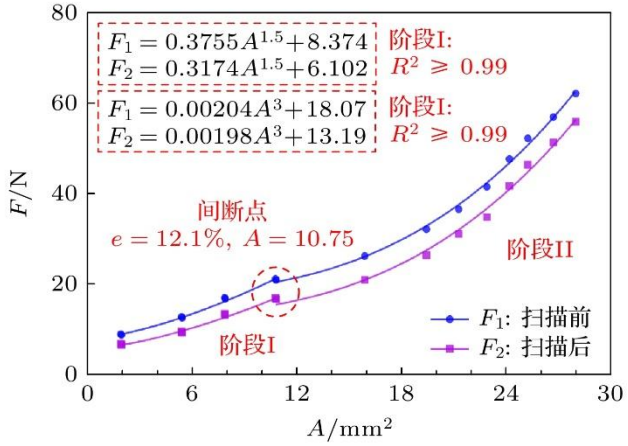

Figure 12. Relationship of contact area A and contact force F.

From the Fig. 12, it can be seen that the contact force increases with the increase of contact area, which can be divided into two stages. When the $\varepsilon \leqslant$12.1%, that is, the $A \leqslant$10.75, the contact force is 1.5 power of the contact area, which is in accordance with Hertz's small deformation contact theory; When 12.1% < $\varepsilon \leqslant$ 28%, i.e. 10.75 < $A \leqslant$ 27.98, the contact force is the cubic power of the contact area, which is in accordance with Tatara's large deformation contact theory.

Take the average value of the coefficients of the fitting formula before and after scanning to obtain:

$$\begin{cases} F_1 = 0.3465A^{1.5} + 7.238,\ A \leqslant 10.75,\ \varepsilon \leqslant 12.1\%, \\ F_2 = 0.002A^3 + 15.63,\ A > 10.75,\ \varepsilon > 12.1\%. \end{cases} \tag{5}$$

In the formula, the precondition $\varepsilon \leqslant$28% is satisfied, that is, $A \leqslant$27.98. The formula is consistent with Hertz's small deformation theory and Tatara's large deformation theory $N=KA^n+B$, where K represents the proportional coefficient of contact area and contact force, which is related to the elastic modulus, Poisson's ratio and diameter of the particle; B represents the offset error, which may be related to the particle material, experimental conditions and other factors.

5. Contact force of three-dimensional granular system

5.1 Pressurized condition of granular system

When the particle system is loaded by the probe, the particles squeeze each other but are not compacted, and the particles still have a relatively high degree of freedom. Fig. 13 shows the change of the pressure *P* of the particle system with the displacement *z* of the indenter during the loading process. The whole loading process is divided into three stages. 1) The pressing displacement *z* = 0 — 6 mm of the loading indenter is stage I. At this time, the particle system is still in the initial state, the indenter does not completely press a particle, and the pressure fluctuates due to the influence of the indenter touching the particle. There is no obvious load transfer characteristic in this stage, so it has no research value. 2) The pressing displacement *z* = 6-14 mm of the loading indenter is stage II. At this time, the probe indenter presses a particle, and the particle is the starting point to continuously transfer the load downward and around. The position of most particles has changed slightly, the particles under the indenter continue to move downward, the particles around the indenter move upward, and the pressure on the system rises gradually. At this stage, the particle system is in a relatively stable stage, showing the characteristics of continuous and slow pressure growth. 3) The downward displacement of the loading indenter *z* = 14 — 20 mm is stage III, when the pressure of the granular system rises sharply and then tends to increase slowly. It shows that the stable state of the previous stage is broken and a new state of particle force chain from destruction to reorganization to stability occurs during the continuous pressing process of the indenter.

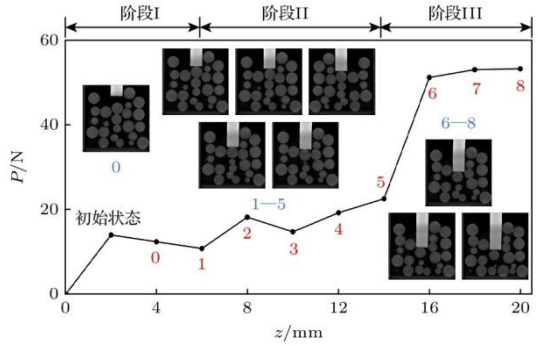

Figure 13. Granular systems pressure situation.

5.2 Contact force calculation

Three-dimensional digital images of particle system were obtained by Mirco-CT experiment, and the contact area *A* between particles was extracted by establishing a pore network model. The relationship between contact force *F* and contact area *A* was established by previous experimental verification, and the contact force *F* between two particles could be obtained by substituting the contact area *A* into the formula. The contact between the particle and the indenter is spherical-planar contact, and the contact force *F* is the load *P* applied by the indenter; the contact between the particles is spherical-spherical contact, and the contact force is calculated by substituting the formula (5) based on the micro-CT double-sphere axial compression experiment. The contact force network distribution of the particle system can be

obtained by calculating all the contact forces between particles, and the evolution of the contact force network distribution under different loading conditions is analyzed. See Fig. 14 for the calculation process.

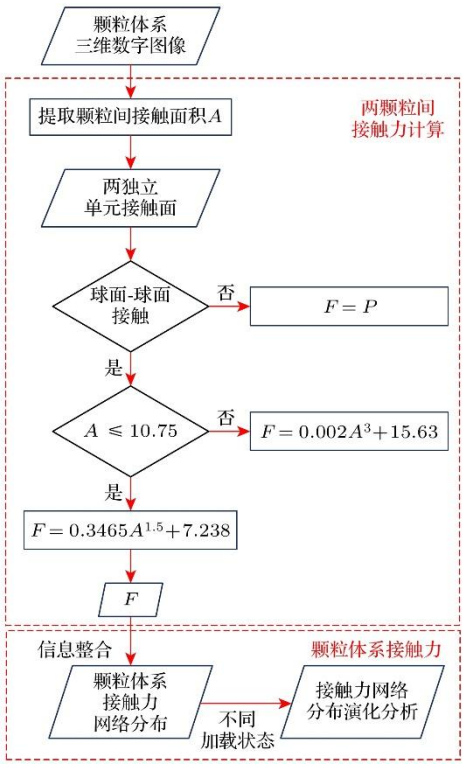

Figure 14. Flowchart for calculation of contact force network distribution and evolution.

5.3 Distribution and Evolution of Contact Force Network

Due to the randomness and disorder of particle distribution, the contact relationship between particles is complex. With the downward movement of the probe indenter, the particles are constantly displaced, and the size and direction of the contact force between particles are updated. The probe indenter contacts the particles as the starting point to continuously transfer the load downward and around. Fig. 15 shows the basic interval and distribution of the contact force of the three-dimensional particle system under different displacement loading. The thickness and color of the network structure in the figure indicate the size of the contact force. It can be seen that the network distribution of the contract force is dynamically updated when the particle system is loaded by the probe. With the downward movement of the probe indenter, the maximum contact force is basically generated at the position of the particle in contact with the indenter, and the nearby particles are deformed and displaced. The overall distribution of the contact force shows that the contact force below the indenter is larger and diverges from the center to the periphery. Particle deformation and movement are accompanied by the loss of energy such as rotation and friction, and the disappearance or generation of contact force occurs in the area near the indenter, and the change of the

magnitude and direction of contact force occurs in some areas. The contact force near the indenter at position 1 in Fig. 15 changes most obviously. During the loading process, the overall value of the contact force increases continuously, and the direction also changes with the movement and extrusion between particles, resulting in the continuous renewal of the contact force. The maximum contact force of 153.86 N occurs at position 2 due to the random rupture and reorganization of the force chain, and the contact force disappears at the next loading state, and the force chain network structure in the nearby region tends to be more stable.

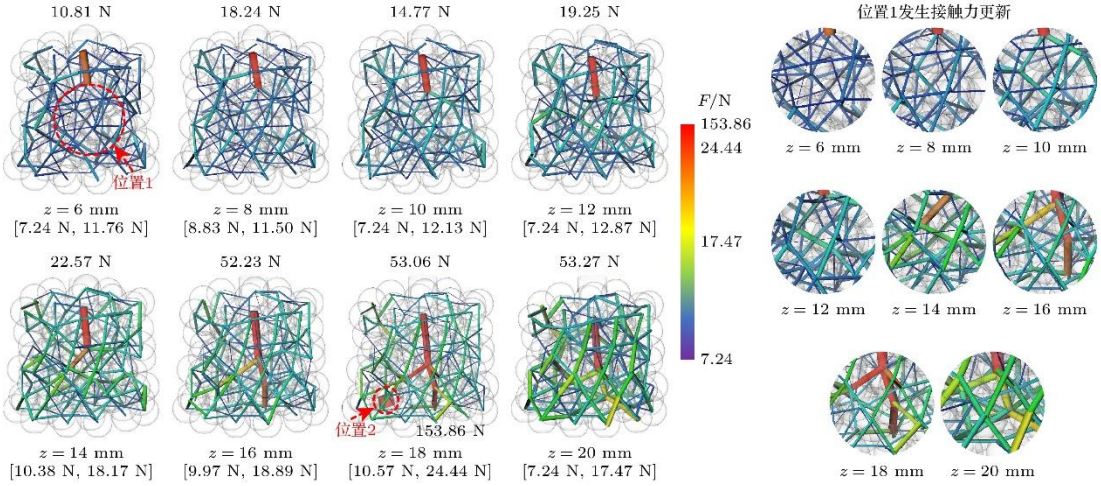

Figure 15. Contact force network distribution and evolution of granular systems.

Fig. 16 shows the range of three-dimensional particle-to-particle contact forces and indentor-particle contact forces at different loading displacements. During the loading process, the contact force between the indenter and the particle is basically the maximum, which is marked near the Fig. 15 indenter; when z = 18 mm, the internal force chain of the particle system is broken and reorganized, and a larger contact force 153.86 N, and is destroyed again in the next loading state, resulting in disappearance. The minimum value of particle contact force interval basically does not change, and the interval changes significantly in stage II and stage III. The overall interval value of stage II is small, and the maximum value of stage III increases and decreases in the final loading state. Combined with Fig. 15, it can be seen that the maximum contact force disappears when z = 20 mm, and the network distribution of contact force is more uniform and stable than the previous state.

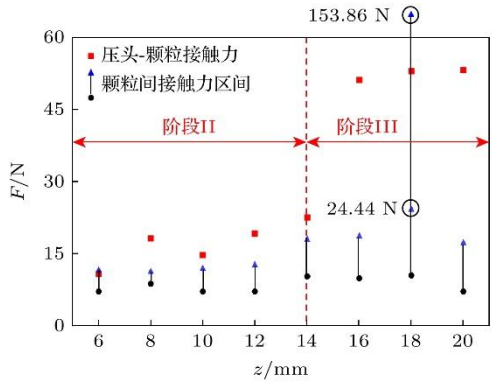

Figure 16. Change in contact force interval.

Fig. 17 shows the variation of the total number of Stage II and Stage III contacts N_T and the average contact force $\bar{F}$ during loading. In stage II, the total number of contacts N_T showed an upward trend; in stage III, the total number of contacts N_T was basically stable around 206, and no significant change occurred. The change trend of the average contact force $\bar{F}$ is consistent with the total number of contacts N_T and, showing an obvious stage change. The more the number of contacts, the more frequent the extrusion between particles, and the greater the contact force between particles, which is stable around 10.5 N in stage III. z = 14 mm is the turning point of stage II and stage III. By comparing the contact force network distribution before and after stage II, it can be seen that the contact force distribution in stage II runs through the total network of the particle system, and the force is uniform; the contact force value at the turning point of stage III is obviously differentiated, and the larger contact force is mainly concentrated below the indenter, which is the center to transmit around.

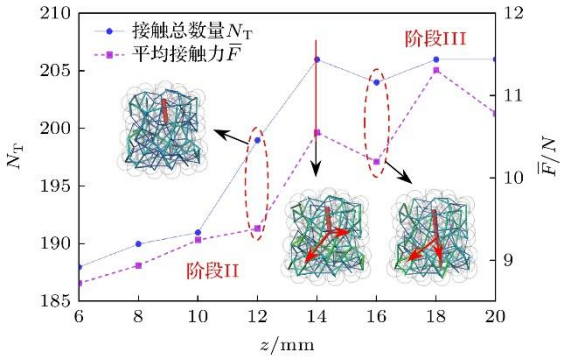

Figure 17. Change in total number of contacts N_T and average contact force $\bar{F}$.

5.4 Distribution and Evolution of Strong Contact Force Network

The strong contact force is defined as the contact force greater than the average contact force in the particle system. As the main support and force transmission structure of the force chain in the particle system, the distribution and development of the strong contact force affect the mechanical characteristics and properties of the whole particle system. Fig. 18 shows the

basic interval and distribution of the strong contact force of the three-dimensional particle system under different displacement loads. The thickness and color of the network structure in the figure indicate the size of the contact force. From Fig. 18, it can be seen that the strong contact force distribution runs through the whole particle system and supports the network structure of the particle system. The larger contact force is mostly concentrated under the probe indenter, and is transmitted and diffused around, and the contact force is gradually reduced outward from the center point. With the continuous pressure of the indenter, the distribution of the strong contact force is more uniform, and the network structure of the whole particle system gradually tends to be stable. The strong contact force at position 1 below the Fig. 18 medium indenter increases as a whole during loading. When z = 18 mm, many old contact forces disappear, and when z = 20 mm, many new contact forces occur.

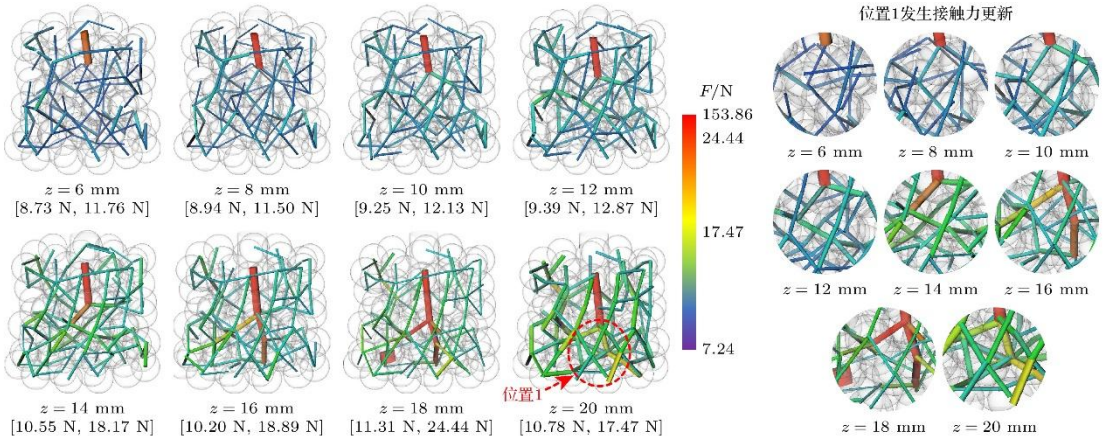

Figure 18. Strong contact force network distribution and evolution of granular systems.

Fig. 19 shows the contact force network distribution of the particle system above the average contact force of 10.78 N in the final displacement loading state. From Fig. 19, it can be seen that the number of contact forces above 10.78 N is gradually increasing. At the beginning, it appears near the cylinder wall, and the structure is scattered; when z = 10 mm, it appears under the indenter, and the tree-like network structure is connected with each other and relatively sparse. With the loading process, the network structure continues to expand, and when z = 14 mm, it covers the whole three-dimensional particle system, and gradually reaches a stable state.

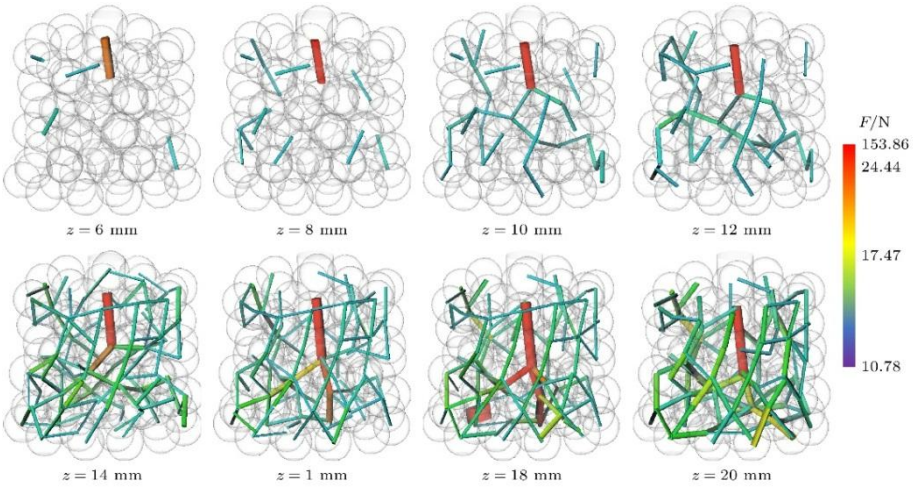

Figure 19. Strong contact force network distribution and evolution more than 10.78 N of granular systems.

Fig. 20 shows the variation of the number of strong contacts N_S above the average contact force $\overline{F}$ and above the average contact force of the final loading state (10.78 N). As the probe indenter is pressed down, the number of strong contacts N_S increases slowly and steadily, and the equilibrium point is established at z = 14 mm. The number of strong contacts N_S changes, showing a trend of first decreasing and then increasing. The establishment of the equilibrium point is also reflected in the change of the pressure on the particle system. At z = 14 mm, the pressure on the particle system increases sharply, indicating that a new contact force network structure with higher bearing capacity is formed at this point. The number of strong contacts N_S above 10.78 N basically reaches its peak, and the main skeleton bearing external load is established. The state of the strong contact force network before and after the equilibrium point is quite different. After the equilibrium point is established, the overall value of the strong contact force is higher, and the distribution of the hard contact force in the particle system is more uniform.

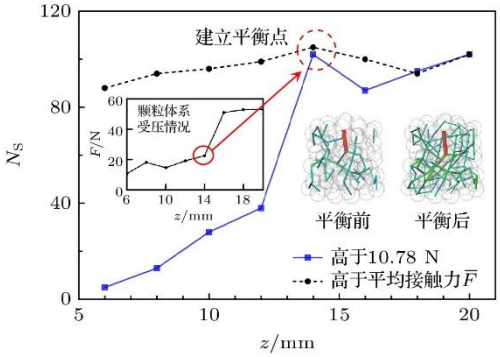

Figure 20. Change in number of strong contacts N_S.

After calculation, the number of strong contacts N_S accounts for 45% -50% of the total number of contacts N_T. Among them, the strong contact, as the main core of the strong force

chain, is to transfer and bear the external load and build the basic skeleton of the particle system, while the weak contact, as the supplement and binder of the network structure of the system, supports the three-dimensional network structure, establishes the connection between particles and maintains the stability of the network structure of the whole particle system.

6. Conclusion

In this paper, the elastic ball contact model is verified based on mirco-CT, and the elastic ball contact force calculation formula suitable for the experimental conditions is obtained. A three-dimensional contact network model of a particle system was constructed by carrying out elastic rubber particle probe loading experiments, and the distribution of particle contact force network during the loading process was obtained. The pressure condition of the granular system is analyzed macroscopically, and the distribution evolution law of the contact force network of the granular system is explored microscopically, and the internal relationship between the number and distribution evolution of strong contacts and the stability of the particulate system is revealed. The main conclusions are as follows.

The main results are as follows: 1) It is verified that the double elastic sphere contact model conforms to Hertz contact theory and Tatara large deformation contact theory, and the fitted contact force formula can reasonably and effectively characterize the contact force between two particles.

2) The whole compression process of the elastic rubber sphere particle system under probe loading can be divided into three stages: initial state, stable compression, and reorganization to stability. In stage I, the pressure head does not press the particle, and the pressure value fluctuates due to the disturbance of the surrounding particles; in stage II, the pressure head presses a particle, and takes the particle as the starting point to transfer the load to other particles in contact with the particle step by step, and the pressure of the particle system increases slowly; in the process of continuous pressing of the pressure head in stage III, the force chain of the particle occurs from destruction to reorganization to a new state of stability, and then the pressure of the particle system tends to increase slowly after a sharp.

3) When the particle system is loaded by the probe, the contact force network distribution is dynamically updated, and the overall contact force distribution shows that the contact force in the area below the probe indenter is larger and diverges from the center to the periphery. The average contact force variation trend is consistent with the number of contacts, showing obvious periodic changes. The more the number of contacts, the more frequent the extrusion between particles, and the greater the contact force between particles, which is stable around 10.5 N in stage III.

4) The distribution of strong contact force runs through the whole particle system and supports the network structure of the particle system. The number of strong contacts

N_S accounts for 45% -50% of the total number of contacts N_T. With the slow increase of loading, the equilibrium point is established at z = 14 mm, and the trend changes, showing a slight fluctuation. At the equilibrium point, it is higher than The number of strong contact forces N_S and of 10.78 N basically reaches the peak, establishing the main skeleton to bear the external load, showing a tree-like distribution under the indenter. After the equilibrium point, the overall value of the strong contact force is higher, and the distribution in the particle system is more uniform.

References

[1] Sun Q C 2015 Acta Phys. Sin. 64 076101

[2] Qu T M, Feng Y T, Wang M Q, Zhao T T, Di S C 2021 Chin. J. Theor. Appl. Mech. 53 2404

[3] Wang Y W, Liu R, Sun R H, Xu Z W 2023 Eng. Comput. 40 1390

[4] Lovoll G, Måløy K J, Flekkoy E G 1999 Phys. Rev. E 60 5872

[5] Blair D L, Mueggenburg N W, Marshall A H, Jaeger H M, Nagel S R 2000 Phys. Rev. E 63 278

[6] Anton K, Neverov S, Neverov A, Dmitry O, Ivan Z, Maria K 2023 Geohazard Mech. 1 128

[7] Lu F, Li Z Y, Yang Z, Zhang L P, Liu J, Li L L, Liu X J 2023 Pet. Geol. Exp. 45 193

[8] Wang S T, Chang Y H, Wang Z F, Su X X 2024 Energies 17 1370

[9] Majmudar T S, Behringer R P 2005 Nature 435 1079

[10] Sanfratello L, Fukushima E, Behringer R P 2009 Granular Matter 11 1

[11] Chen F X, Zhuang Q, Wang R L 2016 Rock Soil Mech. 37 563

[12] Kondo A, Takano D, Kohama E, Bathurst R J 2022 Géotech. Lett. 12 203

[13] Wang X, Chen F X, Wang Y, Liu Y X, Sun J 2023 Chin. J. Theor. Appl. Mech. 55 1732

[14] Hertz H 1881 J. Reine Angew. Math. 92 156

[15] Johnson K L, Kendall K, Roberts A D 1971 Proc. R. Soc. London, Ser. A 324 301

[16] Derjaguin B V, Muller V M, Toporov Y P 1975 J. Colloid Interface Sci. 53 314

[17] Tatara Y 1991 ASME J. Eng. Mater. Technol. 113 285

[18] Tatara Y, Shima S, Lucero J C 1991 ASME J. Eng. Mater. Technol. 113 292

[19] He S M, Wu Y, Li X P 2008 Eng. Mech. 25 19

[20] Yun R D, Ding B 2019 J. Mech. Eng. 55 80

[21] Wu Y, Hao H C, Gao M Z, Gao Z, Gao Y N 2023 Geomech. Geophys. Geo-Energy Geo-Resour. 9 126

[22] Qi J C, Chen R C, Liu B, Chen P, Du G H, Xiao T Q 2017 Acta Phys. Sin. 66 054202

[23] Lubner M G, Ziemlewicz T J, Wells S A, Li Ke, Wu P H, Hinshaw J L, Lee F T, Brace C L 2022 Abdominal Radiology 47 2658

[24] Busch M, Hausotte T 2022 Prod. Eng. 16 411

[25] Mao L T, Bi Y J, Liu H Z, Chen J, Wang J Q, Peng R D, Liu H B, Wu H, Sun Y, Ju Y 2023 Chin. Sci. Bill. 68 380

[26] Sakamoto S, Suzuki K, Toda K, Seino S 2022 Materials 15 7393

[27] Zhuang C, Jianfeng W, Wei X 2023 Géotech. 21 1

[28] Sun Q C, Wang G Q 2008 Acta Phys. Sin. 57 4667

[29] Pérez L G, Bernal P L J, Alés F V, del-Río J J M, Borreguero M, Ochoa J M A 2024 Boletín de la Sociedad Española de Cerámicay Vidrio 63 216

[30] Wu Z H, Yang Y H, Zuo Y J, Meng X R, Wang W T, Lei W L 2023 Acta Geophys. 72 2503

[31] Fang H, He N 2023 Appl. Sci. 13 12270

[32] Lei J, Pan B Z, Zhang L H 2018 Prog. Geophys. 33 653

[33] Hosseinzadegan A, Raoof A, Mahdiyar H, Nikooee E, Ghaedi M, Qajar J 2023 Geoenergy Sci. Eng. 226 211